Journal of MATERIALS RESEARCH

Article
DOI:10.1557/s43578-022-00829-2

Physical and electrochemical characteristics of $NiFe_2O_4$ thin films as functions of precursor solution concentration

Vidyadevi A. Jundale[1,2], Dilip A. Patil[3], Abhijit A. Yadav[1,a)]

[1] Thin Film Physics Laboratory, Department of Physics, Electronics and Photonics, Rajarshi Shahu Mahavidyalaya (Autonomous), Latur, Maharashtra 413512, India
[2] Department of Engineering Science and Humanities, SRES's Sanjivani College of Engineering, Kopargaon, Maharashtra 423603, India
[3] Mechanical Department, Sanjivani KBP Polytechnic, Sanjivani Rural Education Society, Kopargaon, Maharashtra 423603, India
[a)] Address all correspondence to this author. e-mail: aay_physics@yahoo.co.in

Received: 28 August 2022; accepted: 11 November 2022; published online: 28 November 2022

The effects of the precursor solution concentration on the physical and electrochemical characteristics of $NiFe_2O_4$ films were studied. XRD patterns confirmed the formation of a spinel cubic crystal structure. FE-SEM images showed a mesoporous morphology. EDAX analysis confirmed a nearly stoichiometric deposition. Optical absorption studies confirmed the direct bandgap energies in the range 2.00–2.27 eV. The films deposited with a 0.25 M solution concentration had the minimum room-temperature electrical resistivity (3.39×10^3 Ωcm). Films deposited with a 0.15 M solution had the maximum specific capacitance values, 591 F g^{-1} at a scan rate of 5 mV s^{-1} (CV) and 632 F g^{-1} at a current density of 0.5 A g^{-1} (GCD). $NiFe_2O_4$ films exhibited specific energy and specific power values of 15.22 W h kg^{-1} and 225 W kg^{-1}, respectively, at a current density of 1 A g^{-1}. Further, these films retained 92.97% of their specific capacitance after 1000 continuous cycles.

Introduction

Supercapacitors are among the most commonly researched energy storage devices [1–3]. Their energy storage capabilities are several orders of magnitude greater than those of normal dielectric capacitors but significantly less than those of secondary batteries [4]. Among the types of supercapacitors, there are electric double-layer capacitors and pseudocapacitors [5]. Bimetallic oxides are considered promising electrode materials for high-performance pseudocapacitors because their electrochemical activities are higher than those of the corresponding monometallic oxides [6, 7]. Bimetallic oxide materials are highly demanded in comparison to monometallic oxides because they may overcome the limitation of the weak electric conductivity of monometallic oxide materials, achieve a high capacitance and increase the energy density at this capacitor-level power [8, 9]. Bimetallic oxides with a spinel structure (AB_2O_4) are being used to develop pseudocapacitive materials. Here, (A, B) and O represent two dissimilar transition metal cations (Co, Zn, Mg, Mn, Fe, Ni etc.) and the divalent oxygen anion, respectively. The cations can occupy tetrahedral (A) and octahedral (B) sites in a spinel structure, and the O^{-2} anions in a spinel structure form an FCC lattice. A coupling of two metallic oxides enhances the electrical conductivity in a bimetallic oxide, and hence, the electrochemical activity in a bimetallic is greater than the activities of the monometallic oxides [10].

The bimetallic oxide $NiFe_2O_4$ is technologically important because of its high electrochemical stability, tunable conducting behaviour and earth abundance [11, 12]. Generally, the properties of spinel ferrites change with the cationic distribution, chemical composition and synthesis method used [13, 14]. The cationic distribution depends on the synthesis method, type of substitution and particle size [15].

A literature survey showed that even though a lot of research has been done on $NiFe_2O_4$, only a few authors have carried out electrochemical studies of this material. The specific capacitance of $NiFe_2O_4$ is in the range from 18.5 to 677 F g^{-1} [16–21]. Bandgar and colleagues have reported specific capacitance values ranging from 435 to 677 F g^{-1} for thin films of $NiFe_2O_4$ [19]. Even higher specific capacitance values have been reported, but low capacitance retention restricts commercialisation efforts

[21]. In addition, it has been observed that due to oxidation of nickel, nickel oxide (NiO), a secondary phase, is developed on Ni foam [22]. Therefore, it was decided that $NiFe_2O_4$ would be prepared using a simple method, without using carbon or Ni foam or using a high-concentration electrolyte, and that the electrochemical activity would be studied systematically.

The effects of the substrate temperature on the physical and electrochemical properties of $NiFe_2O_4$ thin films have been studied. $NiFe_2O_4$ thin-film electrodes prepared using spray pyrolysis had a maximum specific capacitance of 591 F g^{-1} at 5 mV s^{-1} in a potential window of 0–0.45 V in aqueous 1 M KOH [9]. The electrochemical properties of metal oxides depend on the surface morphology and grain size [19]. The surface morphology is thickness dependent, and the film thickness in turn depends on the concentration of the precursor solution [23]. There are reports in the literature which suggest that the electrochemical properties of metal oxides can be improved through the changes in precursor solution concentration [24–28].

Therefore, $NiFe_2O_4$ thin films were prepared by spray pyrolysis with various solution concentrations at an optimised substrate temperature of 450 °C. The effects of the solution concentration on the structural, morphological, compositional, optical, electrical and electrochemical properties of $NiFe_2O_4$ thin films were studied.

Results and discussion

Film thickness

The photograph of $NiFe_2O_4$ thin films (Fig. S1) prepared using a spray pyrolysis technique with various solution concentrations shows that the brown colour of the $NiFe_2O_4$ thin films becomes darker with increasing solution concentration. This can be ascribed to an increase in film thickness with increasing solution concentration.

The spray-deposited $NiFe_2O_4$ thin films with solution concentrations of 0.05 M, 0.10 M, 0.15 M, 0.20 M and 0.25 M have resultant mass loadings of 0.14, 0.26, 0.36, 0.41 and 0.43 $mgcm^{-2}$, respectively. The film thickness determines the properties of $NiFe_2O_4$ thin films. The thicknesses of the $NiFe_2O_4$ films were found to be 260 nm, 486 nm, 675 nm, 770 nm and 808 nm, corresponding to solution concentrations of 0.05 M, 0.10 M, 0.15 M, 0.20 M and 0.25 M, respectively. Initially, the film thickness increases linearly with increasing solution concentration. This behaviour can be attributed to the increase in the supply of the precursor ions with increasing solution concentration [24, 29]. After 0.20 M, the film thickness increases steeply. The saturation of the film thickness is due to partial thermal decomposition of the spray solution. Similar behaviour was reported previously for spray-deposited F:SnO_2 [30] and $CoFe_2O_4$ thin films [31].

XRD

The crystal structures and internal geometries of the $NiFe_2O_4$ thin films were revealed under XRD. Figure 1 shows the XRD patterns of thin films prepared with various solution concentrations. Diffraction peaks are observed at 30.69°, 35.76°, 37.35°, 43.44°, 53.81°, 57.39° and 62.87°, corresponding to the (220), (311), (222), (400), (422), (511) and (440) planes, respectively. From the figure, it is clear that the thin films are strongly oriented along the (311) plane. A comparison of the calculated and standard '*d*' values confirms that the $NiFe_2O_4$ has a spinel cubic crystal structure with the Fd-3m (227) space group. No impurity peaks were found in the XRD pattern. As seen in the figure, the intensity peaks become broader and sharper with increasing solution concentration. The increased peak (311) intensity signifies that the crystallinity of the $NiFe_2O_4$ films increases with increasing solution concentration. This behaviour can be ascribed to the thermal decomposition of the chemical constituents with rise in solution concentration influencing the growth and crystallinity of the $NiFe_2O_4$ thin films [32].

The lattice parameter of the $NiFe_2O_4$ thin films was determined using the standard relation [33, 34]. The calculated average lattice parameter value ($a = 8.344$ Å) is close to the standard JCPDS data card (86-2267) value ($a = 8.3379$ Å) [35]. The crystallite size of the (311) plane was estimated using the Debye Scherrer formula [34]. It was observed that the crystallite size increases as the solution concentration increases. The crystallite size was observed to be in the range 12–26 nm, which is close to the range of 10–15 nm, reported by Kumar et al. [36] for mesoporous $NiFe_2O_4$ synthesised using the hydrothermal method. The values of the diffraction angle (2θ), interplanar spacing (d), lattice constant (a) and crystallite size (D) of the thin films deposited in this work are given in Table 1.

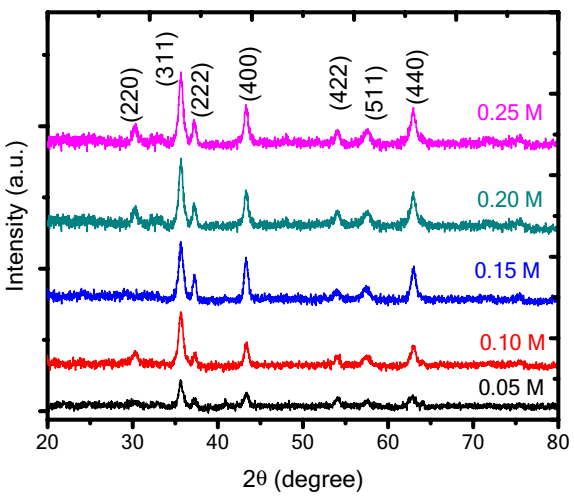

Figure 1: XRD patterns of $NiFe_2O_4$ thin films prepared by spray pyrolysis with various solution concentrations.

TABLE 1: Structural data for $NiFe_2O_4$ thin films prepared by spray pyrolysis with various solution concentrations.

Solution Conc. (M)	2θ (°)	d (Å) (Cal.)	d (Å) (Std.)	hkl	a (Å)	D (nm)
0.05	30.30	2.947	2.849	220	8.3218	12
	35.76	2.509	2.513	311		
	37.35	2.406	2.408	222		
	43.44	2.081	2.085	400		
	53.81	1.702	1.702	422		
	57.39	1.604	1.605	511		
	62.94	1.475	1.476	440		
0.10	30.58	2.921	2.849	220	8.3540	16
	35.63	2.518	2.513	311		
	37.75	2.381	2.408	222		
	43.32	2.087	2.085	400		
	53.81	1.702	1.702	422		
	57.50	1.601	1.605	511		
	63.08	1.472	1.476	440		
0.15	35.51	2.527	2.513	311	8.3360	21
	37.17	2.417	2.407	222		
	43.23	2.092	2.085	400		
	54.15	1.692	1.702	422		
	57.60	1.599	1.605	511		
	62.94	1.475	1.476	440		
0.20	30.33	2.945	2.849	220	8.3548	24
	35.76	2.509	2.513	311		
	37.22	2.413	2.408	222		
	43.58	2.075	2.085	400		
	53.93	1.700	1.702	422		
	57.64	1.598	1.605	511		
	62.94	1.475	1.476	440		
0.25	30.19	2.959	2.849	220	8.3550	26
	35.63	2.518	2.513	311		
	37.30	2.409	2.408	222		
	43.44	2.081	2.085	400		
	54.06	1.695	1.702	422		
	57.77	1.595	1.605	511		
	62.94	1.475	1.476	440		

2θ: Bragg angle, *d*: interplanar spacing, *hkl*: miller indices, *a*: lattice constant, *D*: crystallite size.

FE-SEM

The surface morphology of the $NiFe_2O_4$ thin films was studied using FE-SEM. Figure 2 shows the FE-SEM micrographs (magnification ×300,000) of the films. The films are seen to be crack free. The $NiFe_2O_4$ thin film prepared with a solution concentration of 0.05 M shows a uniform and smooth surface morphology. The thin film prepared with a solution concentration of 0.10 M exhibits a compact morphology with slight agglomeration. The film prepared with a 0.15 M solution concentration exhibits a compact and agglomerated morphology with well-grown, interconnected mesoporous spherical grains of large surface area. Such mesoporous morphology is beneficial for supercapacitor applications. Moradmard et al. [37] have reported a similar spherical grain-type morphology in Al^{3+}-substituted nickel ferrite thin films. The observed morphology may be due to the interaction between the magnetic and nonmagnetic nanoparticles [38] in $NiFe_2O_4$ thin film. The film prepared with a 0.20 M solution had a very dense and compact structure, whereas the film prepared with a 0.25 M solution had a rough surface. The $NiFe_2O_4$ thin films prepared with a 0.15 M solution had an interconnected grain-like surface morphology that is favourable for electrochemical ion intercalation or de-intercalation processes [39].

EDAX

The chemical compositions and stoichiometry of $NiFe_2O_4$ thin films were analysed using EDAX. The EDAX pattern showed

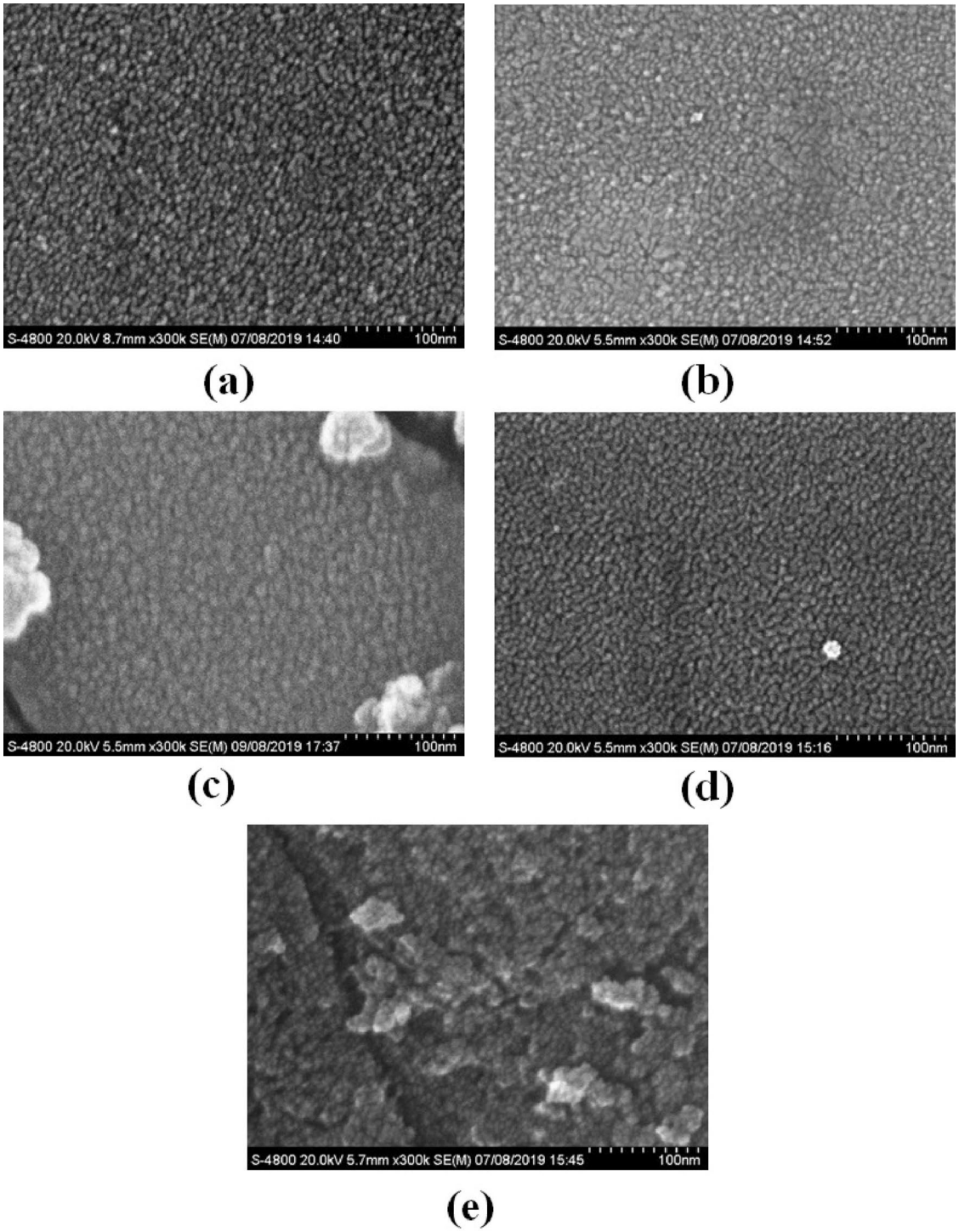

Figure 2: FE-SEM micrographs (magnification ×300 k) for $NiFe_2O_4$ thin films prepared by spray pyrolysis with various solution concentrations (a) 0.05 M, (b) 0.10 M, (c) 0.15 M, (d) 0.20 M and (e) 0.25 M, respectively.

peaks corresponding to nickel (Ni), iron (Fe) and oxygen (O) only. The compositional data of the thin films prepared with various solution concentrations are provided in Table 2. The $NiFe_2O_4$ thin films were stoichiometric.

TABLE 2: Compositional analysis of $NiFe_2O_4$ thin films prepared by spray pyrolysis with various solution concentrations.

Solution Conc. (M)	Atomic percentage in $NiFe_2O_4$ thin films		
	Ni	Fe	O
0.05	11.54	27.63	60.83
0.10	13.05	28.16	58.79
0.15	13.88	28.92	57.20
0.20	14.00	28.32	57.68
0.25	14.89	28.11	57.00

Optical

Optical absorption spectra were recorded in the 400–800 nm wavelength range using a UV–Vis spectrophotometer to measure the bandgap energy of the $NiFe_2O_4$ thin films. The bandgap energy (E_g) of the $NiFe_2O_4$ thin films was estimated using the Tauc's relation [40].

Figure 3(a) shows the variation of $(\alpha h\upsilon)^2$ versus $h\upsilon$. The straight-line nature of the graph extrapolating over a wide photon energy range suggests that the $NiFe_2O_4$ thin films exhibit direct allowed type transitions [40]. The $NiFe_2O_4$ thin films had a high coefficient of absorption, from 10^4 to 10^5 cm^{-1}.The bandgap energy of the $NiFe_2O_4$ thin films was in the range from 2.0 to 2.27 eV. These values are in agreement with the 1.78–2.72 eV range reported by Tong and colleagues [41] for nickel ferrite thin films. Figure 3(b) shows that as the solution concentration increases, the bandgap energy decreases due to increased charge carriers as the bandgap energy is inversely proportional to the natural logarithm of the carrier concentration [42]. The crystallite size also affects the bandgap energy: when the crystallite size increases, the bandgap energy decreases [43], as seen from the XRD results. $NiFe_2O_4$ thin films showed the nano-sized grain-like crystal structure producing a quantum confinement effect. Because of this effect, the bandgap energy may change according to the concentration of the solution used to prepare the $NiFe_2O_4$ thin films. Yadav [44] reported that the solution concentration affects the bandgap energy of tin oxide thin films similarly [44]. The bandgap energy values determined in the present work are provided in Table 3.

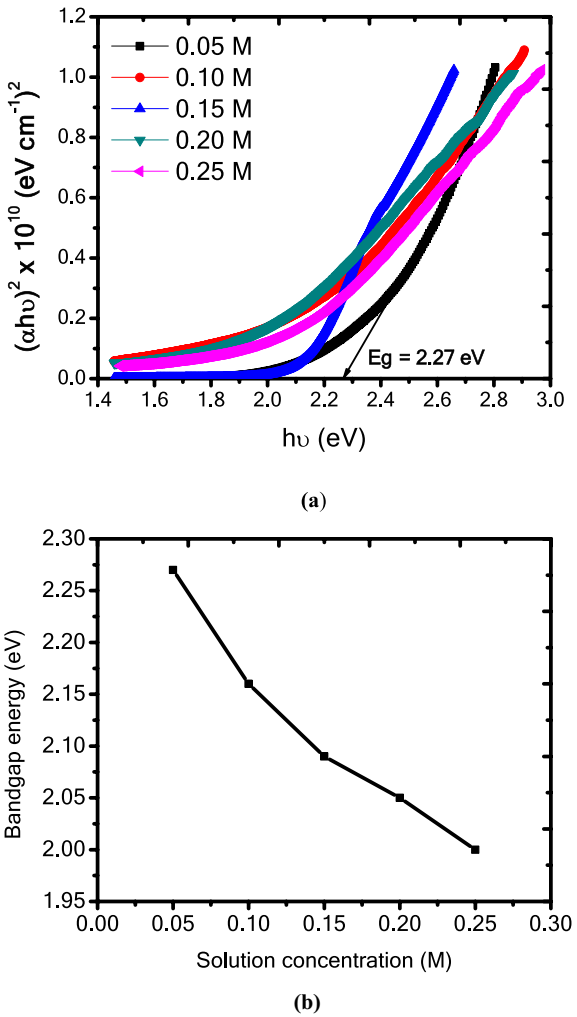

Figure 3: (a) Variation of $(ahu)^2$ versus hu and (b) variation of bandgap energy with solution concentration for $NiFe_2O_4$ thin films prepared by spray pyrolysis.

Electrical resistivity

Electrical resistivity measurements were carried out on the $NiFe_2O_4$ thin films using the DC two-point probe method. Figure 4 shows the variation of log ρ of the thin films with the inverse of the absolute temperature (1000/T). As seen from the figure, the resistivity of the $NiFe_2O_4$ thin films decreases with increasing solution concentration. This behaviour may be attributed to the nanocrystalline behaviour, crystallite boundary irregularities, film thickness, existence of surface states and variations in structural parameters. The decrease in resistivity may depend on the number of defects such as structural disorders, dislocations and surface imperfections

TABLE 3: Optical and electrical properties of $NiFe_2O_4$ thin films prepared by spray pyrolysis with various solution concentrations.

Solution Conc. (M)	Bandgap energy (eV)	Electrical resistivity (Ω-cm)		Activation energy (eV)	
		300 K (×10^3)	500 K (×10^2)	LT	HT
0.05	2.27	243	7.83	0.016	0.032
0.10	2.16	87.1	1.420	0.013	0.023
0.15	2.09	23.4	0.240	0.020	0.025
0.20	2.05	7.24	0.170	0.013	0.021
0.25	2.00	3.39	0.112	0.016	0.021

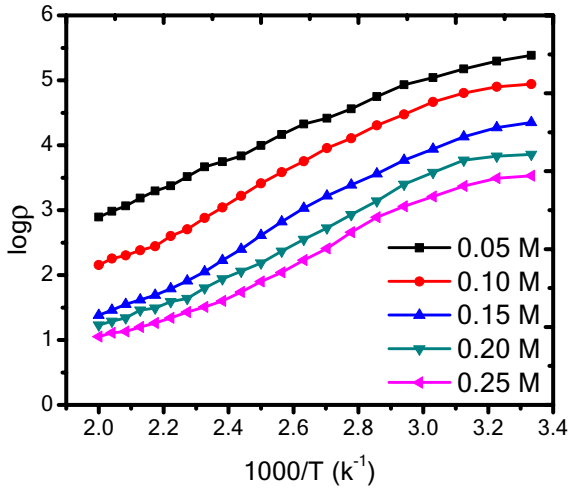

Figure 4: Variation of logρ with inverse of absolute temperature (1000/*T*) for $NiFe_2O_4$ thin films prepared by spray pyrolysis with various solution concentrations.

[45]. The electrical resistivity values of the thin films are provided in Table 3. The observed room-temperature electrical resistivity values of the $NiFe_2O_4$ thin films are in the range 3.39×10^3 Ω cm to 243×10^3 Ω cm, lower than the value of 10^7 Ω cm of $NiFe_2O_4$ nano-sheets deposited from an alkaline bath containing Ni^{2+} and Fe^{2+} ions reported by Gunjakar and co-workers [46].

The activation energies of the $NiFe_2O_4$ thin films were determined using the Arrhenius relation [40]. The activation energies are found to be 0.021–0.032 eV and 0.013–0.020 eV in the high-temperature and low-temperature regions, respectively. Table 3 shows the activation energies of the $NiFe_2O_4$ thin films.

Electrochemical

The effects of solution concentration on electrochemical measurements of the $NiFe_2O_4$ thin films were studied using CV, GCD and EIS. The effect of the scan rate on the specific capacitance of the $NiFe_2O_4$ thin films was studied using CV. The specific capacitance, specific energy, specific power and cycle stability were determined using GCD. The charge transfer resistance was measured using EIS.

CV

The electrochemical behaviour of the $NiFe_2O_4$ thin films was analysed using the CV method and the three-electrode system. CV analysis depends on the thickness of the activated film, concentrations of the precursor solution, surface morphology and scan rate [35, 36]. The curves have two redox peaks (Fig. S2), indicating a faradaic reaction, i.e. pseudocapacitive behaviour of the films [26]. Figure 5(a) shows the CV plots obtained at a scan rate of 10 mV s^{-1} in 1 M KOH. As solution concentration increases up to 0.15 M, the area under the curve increases; thereafter it decreases. The specific capacitance values of the films were determined using a relation given elsewhere [47]. Figure 5(b) shows the variation of specific capacitance with scan rate. The specific capacitance is best (591 F g^{-1}) at a scan rate of 5 mV s^{-1} in the potential window from 0 to + 0.45 V for the films prepared with a solution concentration of 0.15 M. For all the thin films, as the scan rate increases, the area under the curve increases but the specific capacitance decreases. This may

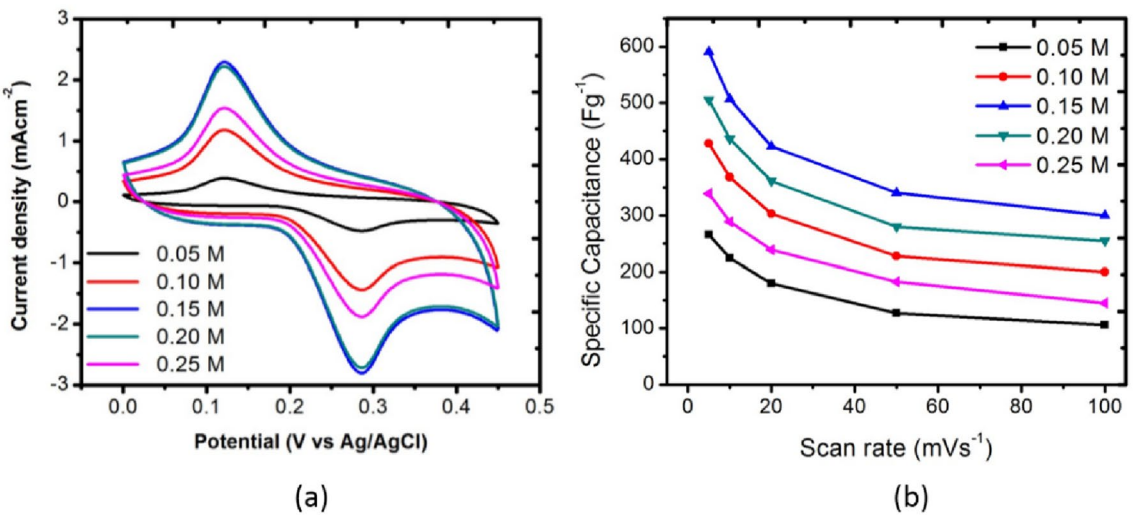

Figure 5: (a) CV plots at scan rate of 10 mV s^{-1} and (b) plot of specific capacitance versus scan rate for $NiFe_2O_4$ thin films prepared by spray pyrolysis with various solution concentrations.

be ascribed to the fact that at higher scan rate, the ions on the electrode move fast and the diffusion of the ions in the electrode is slow [48]. At lower scan rates, outer pores and inner pores are used for ion diffusion [49].

The maximum specific capacitance (591 F g^{-1}) was observed at a scan rate of 5 mV s^{-1} for the $NiFe_2O_4$ thin film prepared with a solution concentration of 0.15 M (Table S1). The thickness of this film was optimal, and a nanocrystalline structure and a mesoporous grain-like surface morphology were observed using XRD and FE-SEM, respectively. The mesoporous morphology provides the electrolyte a wet surface for the diffusion process. Generally, the nano-sized mesoporous $NiFe_2O_4$ has a greater specific capacitance compared with the bulk material [17]. At higher solution concentrations, the specific capacitance decreases due to the increase in the deposited mass. The specific capacitance obtained in the present study is greater than the value of 287 F g^{-1} (in a 1 M Na_2SO_3 electrolyte at a scan rate of 10 mV s^{-1}) reported by Jamadade et al. [50] for an electrosynthesised nickel-doped iron hydroxide thin film with a marigold-like structure, the value of 541 F g^{-1} (scan rate, 2 mV s^{-1}) reported by Bhojane et al. [21] for $NiFe_2O_4$ and the value of 585 F g^{-1} (scan rate, 5 mV s^{-1}) reported by Javed et al. [10] for an NFO-CT solid state supercapacitor.

GCD

The GCD curves of $NiFe_2O_4$ thin films at different current densities are symmetric and nonlinear, indicating the occurrence of an electrochemical faradaic redox reaction due to the interaction between the electrolyte and electrode (Fig. S3). This shows that the $NiFe_2O_4$ thin films exhibit pseudocapacitive behaviour [50,

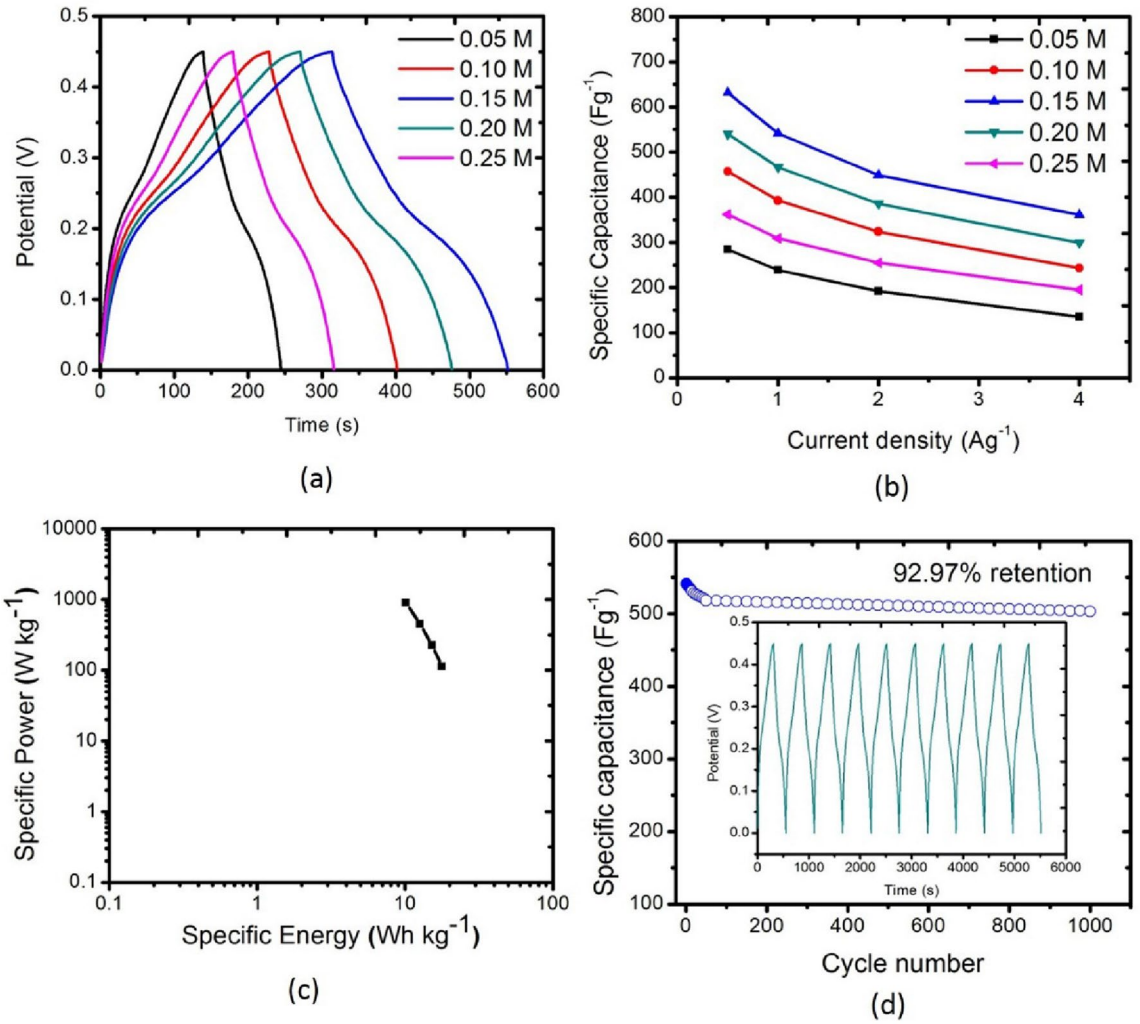

Figure 6: (a) GCD curves at current density of 1 A g^{-1} and (b) plot of specific capacitance versus current density for $NiFe_2O_4$ thin films prepared by spray pyrolysis with various solution concentrations, (c) Ragone plots for $NiFe_2O_4$ thin-film electrode (deposited with 0.15 M solution concentration) supercapacitor and (d) Cycling performance of the $NiFe_2O_4$ thin-film electrode (deposited with 0.15 M solution concentration) at the current density of 1 A g^{-1}. The inset shows the charge–discharge curves of the first 10 cycles of the $NiFe_2O_4$ thin-film electrode.

51]. Figure 6(a) shows the GCD curves of $NiFe_2O_4$ thin films prepared with various solution concentrations at a current density of 1 A g^{-1}. As the precursor solution concentration increases up to 0.15 M, the discharge time increases; as the solution concentration increases further, the discharge time decreases. The specific capacitance, specific energy and specific power were calculated using relations given elsewhere [52].

Figure 6(b) shows the variation of the specific capacitance of the thin films with the current density (Table S2). The maximum specific capacitance is 632 F g^{-1}, at a current density of 0.5 A g^{-1}, for $NiFe_2O_4$ thin film prepared with a solution concentration of 0.15 M. The GCD results are in good agreement with the CV results. The observed specific capacitance of 632 F g^{-1} at a current density of 0.5 A g^{-1} is higher than the value of 137 F g^{-1} at a current density of 1 A g^{-1} reported by Ghasemi and co-workers [53] for $NiFe_2O_4$ nanospheres and the value of 202 F g^{-1} at a current density of 2 mA cm^{-2} reported by Zate et al. [54] for sprayed nickel ferrite.

The specific energy and specific power of the thin films were determined using the equations given in the literature [55]. The specific energy values were plotted against the specific power (Ragone plot) as shown in Fig. 6(c) to evaluate the energy storage performance of the $NiFe_2O_4$ thin-film electrodes. Specific energy and specific power values of 10.15 W h kg^{-1} and 900 W kg^{-1} at a current density of 4 A g^{-1} were found for thin films prepared with a solution concentration of 0.15 M. These values are less than the values of 51.95 W h kg^{-1} and 6.18 kW kg^{-1} reported by Scindia et al. [56] for a NFO/PPy core–shell composite.

Figure 6(d) shows the long-term (1000 cycles) charge–discharge cycle stability of thin films prepared with a 0.15 M solution at a current density of 1 A g^{-1}. The charge–discharge curves of a $NiFe_2O_4$ thin-film electrode for the first 10 cycles are shown in the inset of Fig. 6(d). These show the same symmetric curves. After 1000 continuous charge–discharge cycles, the $NiFe_2O_4$ electrode shows an overall loss of 7.03%, which confirms that the $NiFe_2O_4$ thin film prepared by spray pyrolysis with a 0.15 M solution is structurally very stable. The results indicate that the $NiFe_2O_4$ thin-film electrode exhibits excellent electrochemical stability and reversibility.

EIS

Figure 7 shows the Nyquist plot of the $NiFe_2O_4$ thin films. Z′ represents the ohmic property, and Z″ represents the capacitive property. Generally, there are three parts in a Nyquist plot: a high-frequency region, a middle-frequency region and a low-frequency region. The Nyquist plot has a semicircle in the high-frequency region. The point at which the curve intercepts the real axis gives the solution resistance (R_s) of the electroactive $NiFe_2O_4$ thin film. The EIS studies showed that the lowest electrolyte solution resistance (R_s) and charge transfer resistance

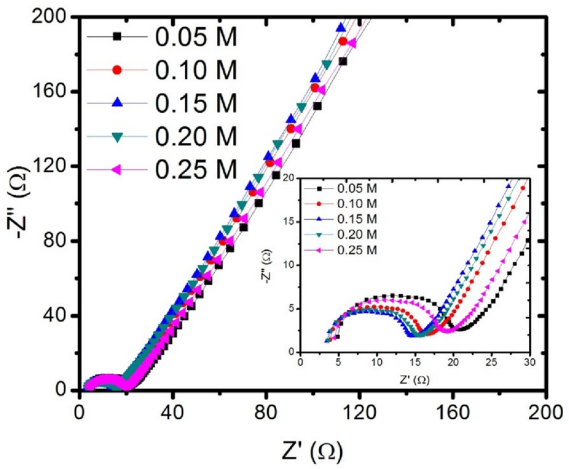

Figure 7: Nyquist plots of $NiFe_2O_4$ thin films prepared by spray pyrolysis with various solution concentrations.

(R_{ct}) of $NiFe_2O_4$ thin films prepared with a solution concentration of 0.15 M were 2.75 Ω and 16.05 Ω cm^2, respectively. The values of R_s are 4.45 Ω, 3.40 Ω, 2.75 Ω, 3.00 Ω and 3.9 Ω for solution concentrations 0.05 M, 0.10 M, 0.15 M, 0.20 M and 0.25 M, respectively. While the values of R_{ct} are 23.05 Ω cm^2, 17.95 Ω cm^2, 16.05 Ω cm^2, 17.05 Ω cm^2 and 21.15 Ω cm^2 for solution concentrations 0.05 M, 0.10 M, 0.15 M, 0.20 M and 0.25 M, respectively. The R_s and R_{ct} decrease with increase in solution concentrations that become minimum at 0.15 M solution concentration and increases thereafter. The results indicate that the thin film prepared with a 0.15 M solution shows better electrochemical performance and that this film can be used for supercapacitor applications [57].

Conclusions

In conclusion, the concentration of the solution used to prepare $NiFe_2O_4$ thin films has substantial effects on the structural, surface-morphological, compositional, optical, electrical and electrochemical properties. The films had a spinel cubic crystal structure. The films were strongly oriented along the (311) direction and had a crystallite size in the range from 12 to 26 nm. FE-SEM images showed a mesoporous spherical grain-like surface morphology without any cracks. EDAX confirmed a nearly stoichiometric deposition. The direct allowed type transition with bandgap energies in the range 2.00–2.27 eV was identified through optical absorption studies. The activation energies were 0.021–0.032 eV and 0.013–0.020 eV in the high-temperature and low-temperature regions, respectively. The $NiFe_2O_4$ thin film prepared with a 0.15 M solution exhibited a maximum specific capacitance of 591 F g^{-1} at a scan rate of 5 mV s^{-1} in the CV study and 632 F g^{-1} at a current density of 0.5 A g^{-1} in the GCD study. Further, the $NiFe_2O_4$ thin film prepared with a

0.15 M solution retained 92.97% retention of its specific capacitance after 1000 cycles at a current density of 1 A g^{-1}. The EIS study showed that the $NiFe_2O_4$ thin film prepared with a 0.15 M solution had a minimum electrolyte resistance of 2.75 Ω and a charge transfer resistance of 16.05 Ω cm^2.

Materials and methods

AR-grade nickel nitrate hexahydrate ($Ni(NO_3)_2{\cdot}6H_2O$) and ferric nitrate nonahydrate ($Fe(NO_3)_3{\cdot}9H_2O$) were used as sources of Ni and Fe, respectively. Solutions of $Ni(NO_3)_2{\cdot}6H_2O$ and $Fe(NO_3)_3{\cdot}9H_2O$ were prepared separately in double-distilled water. Before deposition, 5 ml of the $Ni(NO_3)_2{\cdot}6H_2O$ solution and 10 ml of the $Fe(NO_3)_3{\cdot}9H_2O$ solution were mixed thoroughly by stirring for 15 min to yield a precursor solution. 15 ml of ethanol was added to this precursor solution to make 30 ml of the final spraying solution. The concentration of the $Ni(NO_3)_2{\cdot}6H_2O$–$Fe(NO_3)_3{\cdot}9H_2O$ solution was varied from 0.05 to 0.25 M at 0.05 M intervals. Thin films were deposited with the preparative parameters maintained constant at their optimised values: substrate temperature, 450 °C; spray rate, 3–4 ml min^{-1}; nozzle-to-substrate distance, 30 cm; carrier gas, air and carrier gas pressure, 176 kPa.

The gravimetric weight difference method was used to measure the thickness of the $NiFe_2O_4$ thin films. Phase identification and structural studies of the thin films were carried out using a PW 3710 X-ray diffractometer (Philips) with Cu-Kα radiation (wavelength λ = 1.54056 Å). An FE-SEM (S-4800, Hitachi Corporation, Japan) was used to study the surface morphology of the films. The stoichiometry and material compositions were studied using EDAX. The optical absorption spectra of the $NiFe_2O_4$ thin films were recorded using a UV–Vis spectrophotometer (Shimadzu-1700) to determine the optical bandgap. Electrical conductivity measurements were carried out using the DC two-point probe method. Electrochemical measurements were carried out on the $NiFe_2O_4$ thin films using an electrochemical analyser (CHI 608D). The conventional three-electrode cell configuration system was used, with a 1 cm^2 $NiFe_2O_4$ thin film as the working electrode and platinum and saturated Ag/AgCl as the counter and reference electrodes, respectively, in an aqueous 1 M KOH electrolyte. Electrochemical measurements were made using the cyclic voltammetry and electrochemical impedance spectroscopy techniques. Galvanostatic charge–discharge (GCD) measurements were also made.

Author contributions

All authors contributed to the study conception and design. Material preparation, data collection and analysis were performed by all authors. The first draft of the manuscript was written by VAJ and DAP and AAY commented on previous versions of the manuscript. All authors read and approved the final manuscript.

Data availability

It is hereby assured that materials described in the manuscript, including all relevant raw data, will be freely available to any researcher wishing to use them for non-commercial purposes, without breaching participant confidentiality.

Declarations

Conflict of interests There are no financial or non-financial interests.

Research involving human and/or animal participants

This article does not contain any studies with human or animal subjects.

Supplementary Information

The online version contains supplementary material available at https://doi.org/10.1557/s43578-022-00829-2.

References

1. R. Singhal, M. Chaudhary, S. Tyagi, D. Tyagi, V. Bhardwaj, B.P. Singh, Recent developments in transition metal-based nanomaterials for supercapacitor applications. J. Mater. Res. **37**, 2124–2149 (2022)
2. W. Wang, W.-Y. Xie, F.-X. Zhou, L. Chen, M. Zhou, G.-X. Wang, Xu. Wenyuan, E. Liang, Three-dimensional nitrogen-doped graphene hydrogel-based flexible all-solid-state supercapacitors. J. Mater. Res. **36**, 376–386 (2021)
3. T. Antony Sandosh, A. Simi, Morphology controlled synthesis of one-dimensional $CoMn_2O_4$ nanorods for high-performance supercapacitor electrode application. Chem. Pap. **75**, 2295–2304 (2021)
4. R. Abirami, R. Kabilan, P. Nagaraju, V. Hariharan, S. Thennarasu, Enhanced electrochemical performance of Mn_3O_4/multiwalled carbon nanotube nanocomposite for supercapacitor applications. J. Electron. Mater. **50**, 6467–6474 (2021)
5. A. Dutta, K. Chatterjee, S. Mishra, S.K. Saha, A.J. Akhtar, An insight into the electrochemical performance of cobalt-doped ZnO quantum dot for supercapacitor applications. J. Mater. Res. (2022). https://doi.org/10.1557/s43578-022-00654-7
6. Y. Zhang, C.-R. Chang, H.-l Gao, S.-W. Wang, Ji. Yan, K.-Z. Gao, X.-D. Jia, H.-W. Luo, H. Fang, A.-Q. Zhang, L.-Z. Wang, High-performance supercapacitor electrodes based on $NiMoO_4$ nanorods. J. Mater. Res. **34**, 2435–2444 (2019)

7. X. Zhang, L. Yue, S. Zhang, Y. Feng, L. An, M. Wang, J. Mi, Nickel-doped cobalt molybdate nanorods with excellent cycle stability for aqueous asymmetric supercapacitor. Int. J. Hydrog. Energy **45**(15), 8853–8865 (2020)
8. C. An, Y. Zhang, H. Guo, Y. Wang, Metal oxide-based supercapacitors: progress and prospectives. Nanoscale Adv. **1**, 4644–4658 (2019)
9. V.A. Jundale, D.A. Patil, A.A. Yadav, Preparation and characterization of $NiFe_2O_4$ thin films for supercapacitor applications. Ph. Transit. **95**(11), 786–802 (2022)
10. M.S. Javed, C. Zhang, L. Chen, Yi. Xi, Hu. Chenguo, Hierarchical mesoporous $NiFe_2O_4$ nanocone forest directly growing on carbon textile for high performance flexible supercapacitors. J. Mater. Chem. A **4**, 8851–8859 (2016)
11. S.B. Narang, K. Pubby, Nickel spinel ferrites: a review. J. Magn. Magn. Mater. **519**, 167163 (2021)
12. M. Taei, E. Havakeshian, H. Salavati, M. Azemati, Highly active electrocatalysts for ethanol oxidation based on gold nanodendrites modified with $NiFe_2O_4$ nanoparticles decorated multiwalled carbon nanotubes. Chem. Pap. **73**, 2687–2695 (2019)
13. T. Dippong, F. Goga, E.-A. Levei, O. Cadar, Influence of zinc substitution with cobalt on thermal behaviour, structure and morphology of zinc ferrite embedded in silica matrix. J. Solid State Chem. **275**, 159–166 (2019)
14. C.-H. Yang, Y.-C. Chen, Wu. Chang-Feng, R.-J. Chung, S. Yougbaré, L.-Y. Lin, Novel synthesis of ZIF67-derived $MnCo_2O_4$ nanotubes using electrospinning and hydrothermal techniques for supercapacitor. J. Solid State Chem. **313**, 123351 (2022)
15. Wu. Chenyan, F. Huang, Q. Shen, Yu. LiXin, C. Zhang, J. Sheng, Di. Cheng, H. Yang, Construction of magnetically separable hierarchical Z-scheme $NiFe_2O_4$@$Bi_2Sn_2O_7$ heterojunction with enhanced visible-light photocatalytic activity. J. Mater. Res. **36**, 3366–3379 (2021)
16. Q. Yu, S. Pan, W. Huang, R. Liu, Effects of solution concentration on magnetic $NiFe_2O_4$ nanomaterials prepared via the rapid combustion process. J. Nanosci. Nanotechnol. **19**(4), 2449–2452 (2019)
17. B. Senthilkumar, R.K. Selvan, P. Vinothbabu, I. Perelshtein, A. Gedanken, Structural, magnetic, electrical and electrochemical properties of $NiFe_2O_4$ synthesized by the molten salt technique. J. Mater. Chem. Phys. **130**, 285–292 (2011)
18. M. Sethi, U.S. Shenoy, S. Muthu, D.K. Bhat, Facile solvothermal synthesis of $NiFe_2O_4$ nanoparticles for high-performance supercapacitor applications. J. Mater. Sci. **14**(2), 120–132 (2020)
19. S.B. Bandgar, M.M. Vadiyar, Y.-C. Ling, J.-Y. Chang, S.-H. Han, A.V. Ghule, S.S. Kolekar, Metal precursor dependent synthesis of $NiFe_2O_4$ thin films for high-performance flexible symmetric supercapacitor. ACS Appl. Energy Mater. **1**(2), 638–648 (2018)
20. M. Hua, L. Xu, F. Cui, L. Jiabiao, Y. Huang, J. Bao, J. Qiu, Y. Xu, X. Hui, Z. Yan, H. Li, Hexamethylenetetramine-assisted hydrothermal synthesis of octahedral nickel ferrite oxide nanocrystallines with excellent supercapacitive performance. J. Mater. Sci. **53**(10), 7621–7636 (2018)
21. P. Bhojane, A. Sharma, M. Pusty, Y. Kumar, S. Sen, P. Shirage, Synthesis of ammonia assisted porous nickel ferrite ($NiFe_2O_4$) nanostructures as an electrode material for supercapacitors. J. Nanosci. Nanotechnol. **17**(2), 1387–1392 (2017)
22. V.V. Jadhav, R.M. Kore, N.D. Thorat, J.M. Yun, K.H. Kim, R.S. Mane, C. O'Dwyer, Annealing environment effects on the electrochemical behavior of supercapacitors using Ni foam current collectors. Mater. Res. Express **5**, 125004 (2018)
23. V.R. Shinde, T.P. Gujar, C.D. Lokhande, LPG sensing properties of ZnO films prepared by spray pyrolysis method: Effect of molarity of precursor solution. Sens. Actuators B **120**(2), 551–559 (2007)
24. A.A. Yadav, Preparation and electrochemical properties of spray deposited α-Fe_2O_3 from nonaqueous medium for supercapacitor applications. J. Mater. Sci.: Mater. Electron. **27**(12), 12876–12883 (2016)
25. B.J. Lokhande, R.C. Ambare, R.S. Mane, S.R. Bharadwaj, Concentration-dependent electrochemical supercapacitive performance of Fe_2O_3. Curr. Appl. Phys. **13**(6), 985–989 (2013)
26. A.V. Thakur, B.J. Lokhande, Source molarity affected surface morphological and electrochemical transitions in binder-free FeO(OH) flexible electrodes and fabrication of symmetric supercapacitive device. Chem. Pap **72**(6), 1407–1415 (2018)
27. A. Gahtar, S. Benramache, A. Ammari, A. Boukhachem, A. Ziouche, Effect of molar concentration on the physical properties of NiS thin film prepared by spray pyrolysis method for supercapacitors. Inorg. Nano-Met. Chem. **52**, 1–10 (2021)
28. S. Palanichamy, J. Mohamed, K. ArunKumar, S. Pandiarajan, A. Lourdusamy, Effect of molar concentration on physical properties of spray deposited SnO_2 thin films using nebulizer. J. Sol Gel Sci. Technol. **89**(6), 392–402 (2019)
29. I. Malinowska, Z. Ryżyńska, E. Mrotek, T. Klimczuk, A. Zielińska-Jurek, Synthesis of $CoFe_2O_4$ nanoparticles: the effect of ionic strength, concentration, and precursor type on morphology and magnetic properties. J. Nanomater. (2020). https://doi.org/10.1155/2020/9046219
30. A.A. Yadav, E.U. Masumdar, A.V. Moholkar, K.Y. Rajpure, C.H. Bhosale, Effect of quantity of spraying solution on the properties of spray deposited fluorine doped tin oxide thin films. Phys. B **404**, 1874 (2009)
31. V.A. Jundale, A.A. Yadav, Precursor solution concentration-dependent electrochemical properties of $CoFe_2O_4$ thin films. J. Mater. Sci.: Mater. Electron. **33**(24), 19612–19626 (2022)
32. R.C. Ambare, B.J. Lokhande, Solution concentration and decomposition temperature dependent electrochemical behavior of aqueous route spray pyrolysed Mn_3O_4: supercapacitive approach. J. Mater. Sci.: Mater. Electron. **28**(16), 12246–12252 (2017)
33. V.S. Jamadade, P.K. Pagare, D.S. Gaikwad, A.S. Burungale, V.S. Sawant, Supercapacitive performance of lithium doped and

undoped $NiFe_2O_4$ thin films by chemical deposition method. J. Electron. Mater. **48**, 7539–7542 (2019)

34. S.R. Gibin, P. Sivagurunathan, Synthesis and characterization of nickel cobalt ferrite($Ni_{1-x}Co_xFe_2O_4$) nano particles by co-precipitation method with citrate as chelating agent. J. Mater. Sci.: Mater. Electron. **28**, 1985–1996 (2017)
35. JCPDS data card (86–2267).
36. N. Kumar, A. Kumar, S. Chandrasekaran, T.Y. Tseng, Synthesis of mesoporous $NiFe_2O_4$ nanoparticles for enhanced supercapacitive performance. J. Clean Energy Technol. **6**(1), 51–55 (2018)
37. H. Moradmard, S.F. Shayesteh, The variation of magnetic properties of nickel ferrite by annealing. J. Manuf. Sci. Technol. **3**, 141–145 (2015)
38. A.R. Chavan, S.D. Birajdar, R.R. Chilwar, K.M. Jadhav, Structural, morphological, optical, magnetic and electrical properties of Al^{3+} substituted nickel ferrite thin films. J. Alloys Compd. **735**, 2287–2297 (2018)
39. R.S. Ingole, B.J. Lokhande, Effect of pyrolysis temperature on structural, morphological and electrochemical properties of vanadium oxide thin films. J. Anal. Appl. Pyrolysis **120**, 434–440 (2016)
40. A.A. Yadav, T.B. Deshmukh, R.V. Deshmukh, D.D. Patil, U.J. Chavan, Electrochemical supercapacitive performance of hematite α-Fe_2O_3 thin films prepared by spray pyrolysis from non-aqueous medium. Thin Solid Films **616**, 351–358 (2016)
41. S.-K. Tong, P.-W. Chi, S.-H. Kung, D.-H. Wei, Tuning bandgap and surface wettability of $NiFe_2O_4$ driven by phase transition. Sci. Rep. **8**, 1338 (2018)
42. M. Ardyanian, M. Moeini, H. Azimi Juybari, Thermoelectric and photoconductivity properties of zinc oxide–tin oxide binary systems prepared by spray pyrolysis. Thin Solid Films **552**, 39–45 (2014)
43. M. Oztas, Influence of grain size on electrical and optical properties of InP films. Chin. Phys. Lett. **25**, 4090–4092 (2008)
44. A.A. Yadav, Spray deposition of tin oxide thin films for supercapacitor applications: effect of solution molarity. J. Mater. Sci.: Mater. Electron. **27**(7), 6985–6991 (2016)
45. A.A. Yadav, Nanocrystalline copper selenide thin films by chemical spray pyrolysis. J. Mater. Sci.: Mater. Electron. **25**(3), 1251–1257 (2014)
46. J.L. Gunjakar, A.M. More, K.V. Gurav, C.D. Lokhande, Chemical synthesis of spinel nickel ferrite ($NiFe_2O_4$) nano-sheets. Appl. Surf. Sci. **254**, 5844–5848 (2008)
47. C. Shen, X. Guan, Y. Tang, X. Zhao, Y. Zuo, A zinc-cobalt-nickel heterostructure synthesized by ultrasonic pulse electrodeposition as a cathode for high performance supercapacitors. J. Electroanal. Chem. **902**, 115793 (2021)
48. J. Yan, U. Khoo, A. Sumboja, P.S. Lee, Facile coating of manganese oxide nanowires with high-performance capacitive behavior. ACS Nano **4**, 4247–4255 (2010)
49. A.A. Yadav, U.J. Chavan, Electrochemical supercapacitive performance of spray deposited $NiSnO_3$ thin films. Thin Solid Films **634**, 33–39 (2017)
50. V.S. Jamadade, V.J. Fulari, C.D. Lokhande, Supercapacitive behaviour of electrosynthesized marygold-like structured nickel doped iron hydroxide thin film. J. Alloys Compd. **509**, 6257–6261 (2011)
51. A.A. Yadav, U.J. Chavan, Electrochemical supercapacitive performance of spray deposited NiO electrodes. J. Electron. Mater. **47**, 3770–3778 (2018)
52. Z. Ye, R. Miao, F. Miao, B. Tao, Y. Zang, P.K. Chu, 3D nanoporous core-shell ZnO@Co_3O_4 electrode materials for high-performance supercapacitors and nonenzymatic glucose sensors. J. Electroanal. Chem. **903**, 115766 (2021)
53. A. Ghasemi, M. Kheirmand, H. Heli, Synthesis of novel $NiFe_2O_4$ nanospheres for high performance pseudocapacitor applications. Russ. J. Electrochem. **55**(3), 206–214 (2019)
54. M.K. Zate, S.F. Shaikh, V.V. Jadhav, S.D. Waghmare, D.Y. Ahn, R.S. Mane, S.-H. Han, O.-S. Joo, Electrochemical supercapacitive properties of sprayed nickel ferrite nanostructured thin film electrode. J. Nanoeng. Nanomanuf. **4**(2), 93–97 (2014)
55. Q. Liu, J. Liu, D. Xu, C. Liu, Z. Lu, D. Xuan, Z. Wang, Y. Ye, D. Wang, S. Li, D. Wang, $NiCo_2O_4$ with unique 3D miniature sea urchins as binder-free electrode for high performance asymmetric supercapacitor. J. Electroanal. Chem. **908**, 116068 (2022)
56. S.S. Scindia, R.B. Kamble, J.A. Kher, Nickel ferrite/polypyrrole core-shell composite as an efficient electrode material for high-performance supercapacitor. AIP Adv. **9**, 055218 (2019)
57. B.Y. Fugare, B.J. Lokhande, The influence of concentration on the morphology of TiO_2 thin prepared by spray pyrolysis for electrochemical study. Appl. Phys. A **123**, 394–403 (2017)